RESEARCH ARTICLE

Energy & Environmental Materials WILEY

Lithium-Metal Free Sulfur Battery

Lithium-Metal-Free Sulfur Batteries with Biochar and Steam-Activated Biochar-Based Anodes from Spent Common Ivy

*Pejman Salimi**, *Willem Vercruysse*, *Susana Chauque*, *Saeed Yari*, *Eleonora Venezia*, *Amine Lataf*, *Nahal Ghanemnia*, *Muhammad Shajih Zafar*, *Mohammadhosein Safari*, *An Hardy*, *Remo Proietti Zaccaria*, *and Dries Vandamme**

Lithium-sulfur batteries are emerging as sustainable replacements for current lithium-ion batteries. The commercial viability of this novel type of battery is still under debate due to the extensive use of highly reactive lithium-metal anodes and the complex electrochemistry of the sulfur cathode. In this research, a novel sulfur-based battery has been proposed that eliminates the need for metallic lithium anodes and other critical raw materials like cobalt and graphite, replacing them with biomass-derived materials. This approach presents numerous benefits, encompassing ample availability, cost-effectiveness, safety, and environmental friendliness. In particular, two types of biochar-based anode electrodes (non-activated and activated biochar) derived from spent common ivy have been investigated as alternatives to metallic lithium. We compared their structural and electrochemical properties, both of which exhibited good compatibility with the typical electrolytes used in sulfur batteries. Surprisingly, while steam activation results in an increased specific surface area, the non-activated ivy biochar demonstrates better performance than the activated biochar, achieving a stable capacity of 400 mA h g^{-1} at 0.1 A g^{-1} and a long lifespan (>400 cycles at 0.5 A g^{-1}). Our results demonstrate that the presence of heteroatoms, such as oxygen and nitrogen positively affects the capacity and cycling performance of the electrodes. This led to increased d-spacing in the graphitic layer, a strong interaction with the solid electrolyte interphase layer, and improved ion transportation. Finally, the non-activated biochar was successfully coupled with a sulfur cathode to fabricate lithium-metal-free sulfur batteries, delivering a specific energy density of ~600 Wh kg^{-1}.

1. Introduction

Extensive documentation highlights the detrimental environmental effects of fossil fuels like petroleum, coal, and natural gas, emphasizing the need to shift toward renewable energy sources. However, the primary renewable options, solar and wind energy, are influenced by factors such as day–night cycles, seasonal variations, and weather conditions. The variability in their energy production poses challenges for seamlessly integrating solar and wind technologies into energy grids, as it can lead to hazardous energy production peaks.[1] Nevertheless, it is acknowledged that the utilization of energy storage systems can offer a solution to this problem by capturing excess generated energy, thereby significantly mitigating the risk of grid collapses. In this context, rechargeable batteries, particularly lithium-ion batteries (LIBs), have become prevalent for large-scale electrical energy storage applications,[2] portable devices, and electric vehicles.[3] The state-of-the-art anode material in commercial LIBs is graphite, with a theoretical capacity of 372 mA h g^{-1} which is far below the theoretical capacity of metallic lithium (3860 mA h g^{-1}).[4] In this regard, lithium-sulfur (Li-S) batteries hold the potential to be a more promising energy storage

Dr. P. Salimi, Dr. S. Chauque, Dr. E. Venezia, Dr. M. S. Zafar, Prof. R. Proietti Zaccaria
Istituto Italiano di Tecnologia, via Morego 30, Genoa 16163, Italy
E-mail: pejman.salimi@uhasselt.be
Dr. P. Salimi, Dr. E. Venezia
Department of Chemistry and Industrial Chemistry, University of Genova, via Dodecaneso 31, Genoa I-16146, Italy
Dr. P. Salimi, Dr. W. Vercruysse, Dr. A. Lataf, N. Ghanemnia, Prof. D. Vandamme
Analytical and Circular Chemistry (ACC), Hasselt University, Martelarenlaan 42, Hasselt BE3500, Belgium
E-mail: dries.vandamme@uhasselt.be
Dr. P. Salimi, Dr. W. Vercruysse, Dr. S. Yari, N. Ghanemnia, Prof. M. Safari, Prof. A. Hardy, Prof. D. Vandamme
Institute for Materials Research (imo-imomec), Hasselt University, Martelarenlaan 42, Hasselt BE3500, Belgium
Dr. A. Lataf
Centre for Environmental Sciences (CMK), Hasselt University, Martelarenlaan 42, Hasselt BE3500, Belgium
Prof. M. Safari, Prof. A. Hardy
Energyville, Thor Park 8310, Genk BE3600, Belgium
IMEC Division IMOMEC, Wetenschapspark 1, Diepenbeek BE3590, Belgium
The ORCID identification number(s) for the author(s) of this article can be found under https://doi.org/10.1002/eem2.12758.

DOI: 10.1002/eem2.12758

solution compared to LIBs, offering benefits in terms of cost, environmental impact, energy density, and cycling stability improvements. However, the use of metallic lithium, which plays the role of anode in a Li-S battery, raises some safety concerns, particularly regarding the formation of lithium dendrites during the redox reaction.[5] This critical concern has sparked a search for alternatives to metallic lithium, going toward lithium-metal-free sulfur (LiMFS) solutions, with graphite being the first candidate. LiMFS batteries, unlike the current LIBs, are not dependent on raw materials such as manganese, cobalt, and nickel.[5] This battery technology avoids the use of metallic lithium, providing a safer and longer life cycle in comparison to lithium-based sulfur batteries. Additionally, sulfur with high gravimetrical energy density[6] is naturally abundant, making it a very promising concept for a sustainable battery value chain in many applications, especially for emerging markets such as drones and aviation. Unluckily, it was discovered that graphite does not possess the necessary characteristics to replace metallic lithium due to its poor compatibility with ether-based electrolytes, which happen to be the most common electrolytes used in sulfur-based batteries.[7]

A promising alternative to graphite is biomass-derived carbon, where biomasses such as peanut shells, rice husks, green and brown algae have been employed.[8–13] This kind of carbon, known as biochar, is the solid residue resulting from the pyrolysis procedure,[14] and it has been proven to be suitable for ether-based electrolytes. Biochar can be derived from spent biomass or organic industrial waste. It possesses a non-graphitic/non-graphitizable structure characterized by the presence of heteroatoms (mainly O, N, S, and P), and a disordered configuration of cross-linked carbon sheets.[15] The interesting features of biochar are the adjustable surface area, pore structure, and excellent electronic conductivity.[16] Notably, a life cycle assessment reveals that utilizing waste materials as input for biochar production can yield substantial environmental benefits. Currently, biochars are often under-utilized and end up being incinerated, which disrupts carbon neutrality and causes pollution by releasing CO_2, volatile organic compounds, and oxides into the environment. However, embracing circular economy mechanisms[17] can significantly curb such practices, leading to a more sustainable approach. By doing so, we can address the environmental issues associated with the incineration of biochar and move toward a more environmentally friendly and efficient use of waste materials.

In our earlier research,[18] we showcased the considerable potential of biochar in the context of LiMFS technology, which represents one of the next-generation battery chemistries. In that study, we utilized the brewer's spent grain as an anodic active material, which was then combined with a Li_2S cathode. Owing to the presence of an N- and O-doped biochar, the cell displayed a high capacity of around 350 mA h g^{-1} after 315 cycles in an ether-based electrolyte. Additionally, it has been proven that the refinement of biochars through either steam or CO_2 activation (i.e., activated biochar) could enhance the electrochemical performance of the bio-based electrode in conventional LIBs.[19]

One novel bioresource in a biorefinery system is common ivy, Hedera helix L.[20] Currently, it is used for the preparation of herbal cough-syrups[21] owing to its large content of extractable pharmaceutically active compounds (hederacoside C and α-hederin). Moreover, it is also applied in vertical greenery systems within urban environments, where it has positive effects on air quality,[22] while also reducing the urban heat island effect.[23] These vertical greenery systems require regular trimming, which generates substantial biomass residue streams, indeed an ideal feedstock for high-quality biochar production.[24]

Although numerous reports exist about the application of different kinds of biochars and activated biochars in conventional LIBs, little is given on their electrochemical behavior when applied to next-generation batteries such as LiMFS solutions. In this respect, the main objective of this research is to comprehend the electrochemical behavior of spent common ivy biochar when employed as an anode in LiMFS batteries. Herein, we show that the presence of surficial oxygen functional groups can positively affect the capacity and the cycling performance of the electrodes. The spent common ivy biochar and its steam activated form show different performance in an ether-based electrolyte due to their specific properties, such as the amount of heteroatom contents, degree of graphitization order, and distance between the graphitic layers. In particular, the initial discharge capacity of the non-activated ivy biochar in lithium half-cell configuration is found to be around 1200 mA h g^{-1} (at 0.1 A g^{-1}) with 87% capacity retention during 450 cycles at 0.5 A g^{-1}. Under the same conditions, the steam-activated ivy biochar demonstrated an initial capacity of 1000 mA h g^{-1} with a capacity retention of 80%, once again highlighting the different effects associated with the activation process.

2. Results and Discussion

2.1. Structural Characterization

The CHNS elemental analysis of the ivy biochar (IB) and steam activated ivy biochar (SAIB) is shown in **Table 1**. As reported in the literature,[25] the activation process based on steam entails oxidation reactions via the diffusion of steam through the porous network, resulting in an increase in porosity. Therefore, SAIB shows lower nitrogen and oxygen contents compared to IB. This is because the activation process leads to the removal of heteroatoms and increases the carbon content. After the activation process, a large decrease in the O/C, N/C, and H/C ratios was observed. Greater O/C and N/C ratios indicate higher doping and surface polar functional groups, which improve the hydrophilicity of the biochar, while a higher H/C ratio predicts more aromatization in the structure of the biochar. In a previous work of ours,[19] we observed that a high content of oxygen and nitrogen can reduce the stability of the electrode when immersed in conventional LIB electrolytes, which would negatively affect its electrochemical response. In turn, it was concluded that steam activation was indeed an important procedure for improving conventional LIBs performance.

The functional groups in the two samples were first identified by the fourier-transform infrared (FTIR) method (**Figure 1a**), confirming their lignocellulosic nature. The IR profiles of the activated and non-activated biochars are indeed very similar. The peaks at around 2925 and 2855 cm^{-1} are associated with CH_2 asymmetric and symmetric stretching,[26] while the peaks between 1950 and 2180 cm^{-1} are related to carboxyl and carbonyl groups.[19] Proceeding toward lower wavenumbers, at around 1740 cm^{-1} is identified a peak indicative of the C=O stretching vibration (lignin and hemicellulose)[27] and

Table 1. CHNS elemental analysis of IB, and SAIB samples.

Sample	C [%]	N [%]	H [%]	S [%]	O [%]	Ash [%]	H/C	O/C	N/C
IB	76.46	1.94	1.77	—	11.72	8.11	0.023	0.15	0.025
SAIB	79.40	0.94	0.88	1.75	4.70	11.41	0.011	0.07	0.011

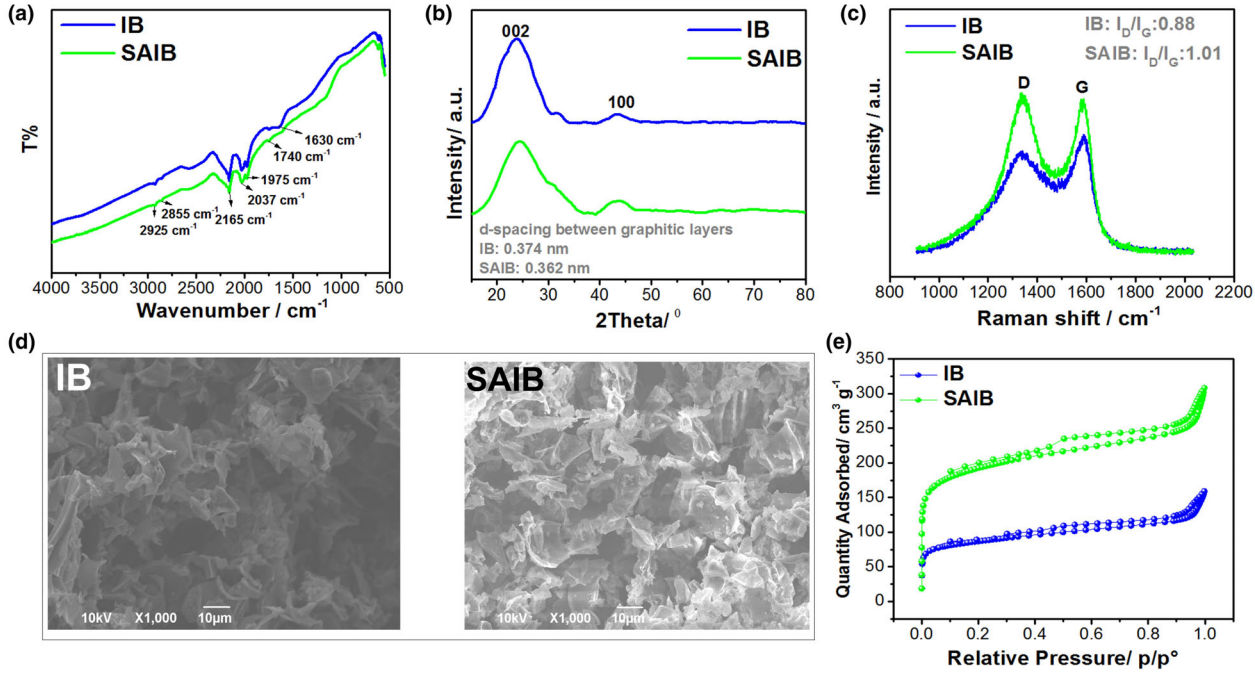

Figure 1. a) FTIR spectra, b) XRD patterns, c) Raman spectra, and d) SEM images of IB and SAIB. e) Nitrogen adsorption–desorption isotherms of IB and SAIB.

at 1630 cm^{-1} another peak, which is more intense in the IB than in the SAIB sample, describes the NH_2 deformation in primary amides.[28] Finally, the peaks between 1100 and 1300 cm^{-1} are associated with residual signals of C–O–C holocellulose, syringyl, and C–O stretch in lignin and xylan.[29,30] It should be noted that some peaks are also identified below 1000 cm^{-1}, corresponding to aromatic C–H out of plane bending vibration.[31,32]

Figure 1b exhibits the X-ray diffraction (XRD) patterns of the IB and SAIB samples, which are similar to the patterns observed in most disordered carbon materials.[33] There are two distinct broad diffraction peaks at ∼24° and ∼44° that are related to the (002) and (100) reflection planes, respectively.[34] Based on Bragg's law ($\lambda = 2d_{002} \sin\theta$),[35] the interlayer distance among the graphitic layers (d_{002}) is calculated for both samples. In particular, the average graphitic interlayer spacing of IB yields a value of 0.374 nm, which is ∼3% larger than the interlayer spacing of SAIB (0.362 nm). The reduction in the average graphitic interlayer spacing following biochar activation results from complex structural and chemical transformations induced by the activation process. These transformations encompass the removal of heteroatoms, the establishment of a porous structure, and chemical alterations.[36] For instance, as evident from CHNS analysis (Table 1), activation leads to a notable reduction in the quantity of heteroatoms, such as O and N. Finally, the XRD patterns reveal other peaks that can be related to some inorganic phases, including crystalline SiO_2 (ICSD 83849) and trydimite (ICSD 176), the typical contaminations found in quartz reactors.

In addition to FTIR and XRD, IB and SAIB samples were further analyzed by Raman spectroscopy with a 532 nm laser excitation source with the intent to identify the changes in the carbon microstructures due to the activation process (Figure 1c). The IB and SAIB spectra show indeed two different amplitudes associated with the peaks located at ∼1335 and ∼1584 cm^{-1}. The peak at 1335 cm^{-1} refers to the D band, describing the disordered structure/defects of the samples,[37] while the 1584 cm^{-1} peak is related to the G band, corresponding to the stretching vibration of sp^2 carbon plane.[38] It is observed that the activation process results in an increase in both peaks amplitudes, where the D band increase is possibly due to the formation of aromatic methyl structure.[39] Furthermore, the intensity ratio I_D/I_G increases from 0.88 to 1.01 after activation, indicating that IB contains more C=O or C=C groups,[40] suggesting that IB is characterized by a higher graphitic order than SAIB.

The monographs of the non-activated and activated biochars were obtained by scanning electron microscopy (SEM). Figure 1d shows that both samples have a heterogeneous, rough, and uneven surface; namely, no specific differences have been identified between the IB and SAIB samples. However, Figure 1e illustrates the nitrogen physisorption profile of both samples, with the typical profile of a micro/mesoporous activated carbon with a slit-like pore structure.[41] Indeed, this analysis was carried out to determine the surface area and porosity of both samples, resulting in the contemporary presence of micro and mesoporous structures, as suggested by the combination of type I and type IV (IUPAC classification) with an evident type of H4 hysteresis loop. The figure also highlights an important difference in the response between IB and SAIB, with the latter being more prone to accepting N_2 gas, namely characterized by a higher surface area than IB.

According to the Brunauer–Emmett–Teller (BET) surface analysis, the specific surface areas (SSA) of IB and SAIB are equal to 284.8 and 627.6 $m^2 g^{-1}$, respectively. It is worth noting that in both cases the dominant pore is micropore, with contributions S_{micro} equal to 248.8 and 557.5 $m^2 g^{-1}$ for IB and SAIB, respectively. The pore size distribution curves of the IB and SAIB samples, measured by N_2/CO_2 adsorption and desorption, are demonstrated in Figure S1, Supporting Information. This analysis reveals a very similar pore distribution

between the two samples, comprising both micropores (<2 nm) and small mesopores (2–10 nm). It is worth mentioning that in the case of ivy biomass, pyrolysis at 700 °C is high enough to achieve a porous structure with a relatively high surface area.[42]

Transmission electron microscope (TEM) and energy-dispersive X-ray spectroscopy (EDX) analyses of both the IB and SAIB samples are also provided in Figure S2, Supporting Information. The dark-field image of the IB sample in Figure S2a, Supporting Information reveals a compact surface with particle aggregation on the carbon sheet, whereas Figure S2b, Supporting Information illustrates the more porous structure of the SAIB sample resulting from the activation process, as highlighted by BET analyses. The EDX maps of IB (Figure S2c, Supporting Information) demonstrate the aggregation of heteroatoms, as observed in the dark-field TEM images (Figure S2a, Supporting Information), and a homogeneous dispersion of other minor elements on the particle surface. The main components, in addition to carbon, include O, P, Ca, and Fe, with lesser amounts of Si, S, Mg, Mn, and Ni. The EDX maps of SAIB are presented in Figure S2d, Supporting Information, where the relevant elements along with carbon are O, P, Ca, and Si, while K, S, Mg, Fe, F, and Cl are also present, all uniformly distributed within the sample.

2.2. Electrochemical Characterization of IB and SAIB Electrodes

The electrochemical performance of the non-activated and activated biochars has been evaluated through the following electrochemical techniques: cyclic voltammetry (CV), galvanostatic charge/discharge, electrochemical impedance spectroscopy (EIS), and galvanostatic intermittent titration technique (GITT). In this respect, **Figure 2**a,b depict the CV curves of the IB and SAIB electrodes in half cell configuration (vs metallic lithium) at a scan rate of 0.1 mV s^{-1}. During the first reduction cycle, two peaks appeared in the IB electrode (at ~2.25 and 1.8 V), which are related to the irreversible reaction of the ether-based electrolyte with the surface functional groups of IB.[43] Importantly, these peaks are too small to be observed in the SAIB plots (Figure 2b), hence suggesting the existence of more heteroatoms such as oxygen and nitrogen[43] in IB than in the SAIB electrode. Moreover, the analysis shows two redox peaks for both IB and SAIB electrodes at about 0.01 V (cathodic peak) and 0.2 V (anodic peak), which represent the lithiation and de-lithiation of the electrodes, respectively.[10] Similarly, both electrodes exhibit a broad reduction peak at around 0.7 V, indicating the formation of the solid electrolyte interphase (SEI) film on the electrode surface.[44] We notice that this peak has not disappeared in the subsequent cycles (particularly for the SAIB electrode), which is attributed to the incomplete stabilization of the SEI layer during the first reduction cycle.

Proceeding with the analysis of Figure 2a,b, a broad oxidation peak at around 1.1 V can be observed for both samples, even though it is better expressed in the IB electrode. This peak could be related to a reaction between the surface oxygenic functional groups and Li^+.[45] Finally, an irreversible peak at 1.5 V can be easily identified, being related to $LiNO_3$ decomposition.[46] Worth noting, the CV curves of both electrodes return almost overlapping curves from the 3rd to the 10th cycle, suggesting a good reversibility of the redox processes.

CV experiments were also performed by decreasing the scan rate from 5 mV s^{-1} down to 1 mV s^{-1} (see Figure S3, Supporting Information) in order to calculate the contribution of the surface (non-faradaic current) and bulk (faradaic current) processes to the overall current. Firstly, as expected, by decreasing the scan rate, the peak intensity decreases as well due to the presence of a thicker diffusion layer.[47] Secondly, it is well known that the capacitance varies linearly with the potential scan rate (ν), expressed by the term $k_1\nu$, while the faradaic contribution depends on the root square of the scan rate as $k_2\nu^{1/2}$. The overall current results to be:[48,49]

$$i(V) = k_1\nu + k_2\nu^{1/2} \quad (1)$$

which leads to

$$\frac{i(V)}{\nu^{1/2}} = k_1\nu^{1/2} + k_2 \quad (2)$$

From the linear fits of the quantity $i/\nu^{1/2}$ versus the scan rate ν, the current contributions related to the faradaic and non-faradic processes can be obtained. In this regard, Figure S4, Supporting Information depicts the results of these calculations for the CV at 1 mV s^{-1} for both IB and SAIB electrodes. Figure S4, Supporting Information also shows the experimental CV at the same scan rate, evidencing a good overlap between the calculated and experimental data. The main aspect to highlight is that in both cases, the faradaic current (bulk reaction) is the most dominant process.

The galvanostatic charge–discharge profiles of both samples are provided in Figure 2c,d. The non-activated and activated biochars show

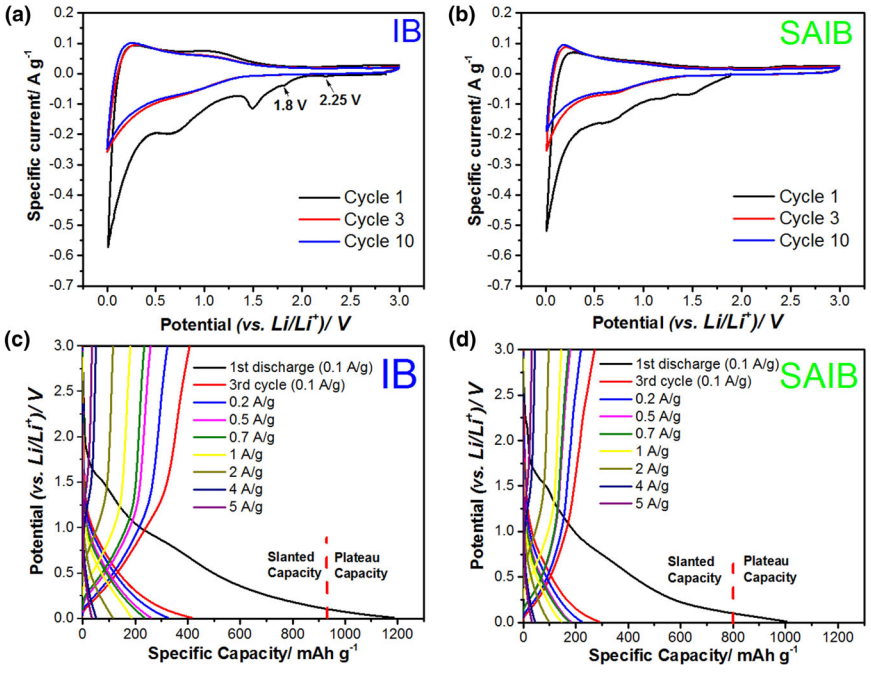

Figure 2. a, b) CV curves of IB and SAIB electrodes at the scan rate of 0.1 mV s^{-1}, c, d) Galvanostatic charge–discharge profiles of IB and SAIB electrodes, performed in lithium-metal half cells at room temperature within 0.01–3.00 V. Electrolyte: DOLDME-LiTFSI-$LiNO_3$.

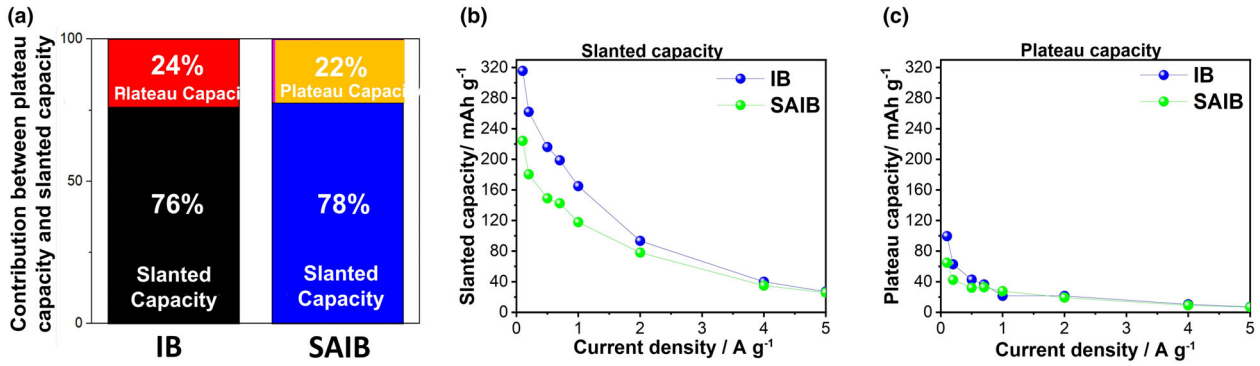

Figure 3. a) Capacity contribution associated with the IB and SAIB electrodes. b) Slanted capacity (>0.1 V) and c) plateau capacity (<0.1 V) of the electrodes at various current densities. All these data have been evaluated for the 3rd discharge cycle in Figure 2c,d.

an initial discharge capacity at 0.1 A g^{-1} of 1185 and 1004 mA h g^{-1}, respectively. The initial coulombic efficiencies (ICE) of the IB and SAIB electrodes read 40% and 31%, respectively, and keep increasing up to 99% in a few cycles. The lower ICE of the SAIB electrode could be caused by the higher SSA of the activated biochar, which would promote an excessive amount of electrolyte decomposition at low potentials. Indeed, although a high surface area can be beneficial for adsorption and ion storage, it can also lead to a significant consumption of ions during the process of filling the pores during the initial cycles. In this respect, it should be mentioned that low ICE is a typical characteristic of turbostratic porous carbon structures.[50] Additionally, and as expected, by increasing the current density from 0.1 to 5 A g^{-1}, the specific capacity lowers due to the corresponding polarization increase.

Figure 3 reveals the discharge capacity contributions in two specific potential ranges, named slanted and plateau (see Figures 2c,d and 3b, c). Both electrodes behave similarly (Figure 3a), even though the largest contribution to the total capacity can be associated with the slanted capacity (>0.1 V) compared to the plateau capacity (<0.1 V). According to recent studies, the high-potential slanted region could be related to ion adsorption associated with the presence of defects/edge sites and functional groups, while the low-potential plateau region is associated with ion intercalation into the graphitic layers of the carbon-based electrodes.[51,52] From Figure 3a, it appears that the dominant storing mechanism is lithium-ion adsorption on defects and edge sites of the carbon surface in both IB and SAIB electrodes. Herein, the IB sample presents a slightly larger contribution of plateau capacity than the SAIB electrode which could be related with the higher degree of graphitization in IB (Figure 1c). Furthermore, Figure 3b,c demonstrates that both slanted and plateau capacities decrease by increasing the current densities due to the higher cell polarization. Interestingly, at low current densities (<2 A g^{-1}), the IB electrodes return slanted and plateau capacities higher than for the SAIB electrodes, whereas they tend to coincide at high current densities (>2 A g^{-1}). This behavior can be understood by recalling that a under fast charge/discharge process, there is not sufficient time to intercalate/reaction lithium ions into the graphitic layer, defects/edge sites, and functional groups; therefore, the effect associated with slanted and plateau capacities tends to normalize. This is confirmed by **Figure 4**a, which depicts the rate performance of IB and SAIB electrodes during cycling at various current densities. Indeed, the specific discharge capacity of IB is around 390 (0.1 A g^{-1}), 325 (0.2 A g^{-1}), 260 (0.5 A g^{-1}), 235 (0.7 A g^{-1}), 188 (1 A g^{-1}), 112 (2 A g^{-1}), 50 (4 A g^{-1}), and 34 mA h g^{-1} (5 A g^{-1}), respectively. On the other hand, the SAIB electrodes present specific discharge capacity values around 272 (0.1 A g^{-1}), 224 (0.2 A g^{-1}), 181 (0.5 A g^{-1}), 175 (0.7 A g^{-1}), 145 (1 A g^{-1}), 97 (2 A g^{-1}), 44 (4 A g^{-1}), and 32 mA h g^{-1} (5 A g^{-1}). At all current densities, the non-activated electrodes offer higher reversible capacities. This could be related to the presence of a higher amount of heteroatoms in the IB structure and the larger *d*-spacing in the graphite layer of IB (0.374 nm for IB against 0.362 nm for SAIB), which provide more active sites for lithium adsorption and diffusion. Additionally, when the current density returns to 0.1 A g^{-1} after cycling at different current values, the IB electrodes show no capacity drop (compared to 10th cycle at 0.1 A g^{-1}), whereas SAIB is affected by a 4% capacity reduction. However, at current densities higher than 1 A g^{-1}, the delivered capacities of IB and SAIB are very close.

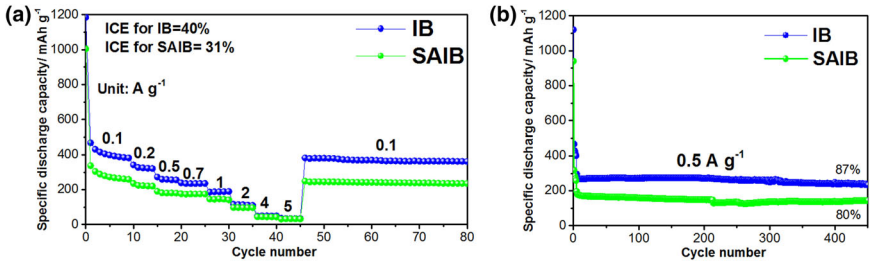

Figure 4. a) Rate capability of the IB and SAIB electrodes over cycling at various current densities (A g^{-1}), and b) cycling performance (current density of 0.5 A g^{-1}) of the samples performed in lithium-metal half cells and activated at low current density at room temperature within 0.01–3.00 V. Electrolyte: DOLDME-LiTFSI-$LiNO_3$. ICE, initial coulombic efficiency.

Figure 4b describes the cycling performance of the electrodes at 0.5 A g^{-1} (equivalent to ~1.4 C for graphite electrode) in lithium-metal half cells when a standard electrolyte (DOLDME-LiTFSI-$LiNO_3$) for sulfur batteries is employed. Owing to their porous nature, it is well known that biochar-based electrodes expand in volume when lithium ions embed via redox reactions. Moreover, the biochar structure will be altered, such as by collapsing, when the lithium ions are released from the substance.[53] Compared to bulk materials (such as graphite), this structural collapse of porous

materials happens more readily, requiring some time to stabilize. Herein, it is found that at the 10th cycle (at 0.5 A g^{-1}), the specific discharge capacities of IB and SAIB remain constant at 268, and 173 mA h g^{-1}, respectively. The cells with non-activated and activated biochars exhibit average specific discharge capacities of 260.8, and 147.1 mA h g^{-1} during the first 450 cycles, respectively. Additionally, the capacity retention is 87% and 80% for Li/IB and Li/SAIB cells, respectively.

For better understanding the electrochemical behavior of the IB and SAIB electrodes in the ether-based electrolyte, EIS analysis was carried out during cycling (at 0.5 A g^{-1}) to determine the resistance of the SEI film (R_{sei}). The impedance spectra of the cells are depicted by the Nyquist plots (Figure S5a,b, Supporting Information), which include two semicircles and a long-inclined line (Warburg impedance) at high and low frequencies, respectively. The numerical values of the R_{sei} were calculated according to the equivalent circuits reported in our previous work.[18] Although both kinds of electrodes demonstrate very low R_{sei} variation upon cycling (Figure S5c, Supporting Information), IB electrodes show a more stable film formation, which could be related to the strong interaction between the surface oxygen functional groups of IB and the SEI layer. These electrodes also show a lower charge transfer resistance at the electrode–electrolyte interface than the SAIB electrodes (second semi-circle), together with a smaller overall impedance (size of the semi-circles).

The swelling of the electrodes due to the electrolyte was investigated by evaluating the contact angle (**Figure 5**). The IB electrode shows a rapid wetting behavior ($\theta = 15°$) toward the electrolyte, whereas the SAIB electrode displays a lower wetting response ($\theta = 26°$). These findings reveal that the oxygen and nitrogen functional groups are beneficial to lithium-ions insertion/de-insertion into/from biomass-based electrodes during discharging and charging. In turn, this explains why the cells prepared by employing the IB electrode, characterized by a higher quantity of oxygen functional groups than the SAIB electrode, show higher capacity together with excellent stability.

To further understand the electrochemical behavior of IB and SAIB anodes, GITT was used to investigate the lithium-ion diffusivity in each structure. Figure S6, Supporting Information displays the GITT profiles of the IB and SAIB electrodes for the eleventh discharge–charge cycle at a pulse current of 50 mA g^{-1} for 10 min with rest intervals of 2 h. Based on a simplified solution of the one-dimensional transport subject to finite-space conditions, the lithium diffusivity (D_{Li^+}) can be approximated by using the equation:[40,54]

$$D = \frac{4}{\pi \tau}\left(\frac{m_B V_m}{M_B S}\right)^2 \left(\frac{\Delta E_s}{\Delta E_t}\right)^2 \quad (3)$$

where m_B is the mass of each active material, V_m is the molar volume of the material (here the molar volume of hard carbons was considered, 8 cm^3 mol^{-1}), M_B is the molar mass of carbon (12 g mol^{-1}), S is the contact surface area of the electrode (1.25 cm^2), τ is the current pulse duration (10 min), ΔE_s is the steady-state potential change, and ΔE_t is the potential change during the current pulse application. **Figure 6** shows, for both kinds of electrodes, the behavior of D_{Li^+} during the discharge (lithiation) (a) and charge (de-lithiation) (b) processes together with the derivative of the galvanostatic charge/discharge at the 10th cycle. The results return a lower apparent diffusion coefficient for the lithiation process, suggesting that lithiation could be less effective at high C-rate cycling.

The D_{Li^+} continuously decreases with the progress of lithiation, which can be ascribed to the increased cross-interactions among the lithium and host in a concentrated system (Figure 6b). The D_{Li}, however, decreases with a non-monotonic trend with the progress of de-lithiation (Figure 6a). This might be explained by a multiplicity of the energetic levels of the lithiated sites, with the delithiation of lithium ions starting from the less energetic sites at lower potential, followed by a more difficult delithiation from the more energetically favorable sites at higher potential.[55] The different trends of variation in D_{Li^+} between the lithiation and de-lithiation steps might suggest a difference between the mechanistic details of the lithiation and delithiation steps in our electrodes, which needs further investigation going beyond the scope of the present work. Comparing both materials, we have

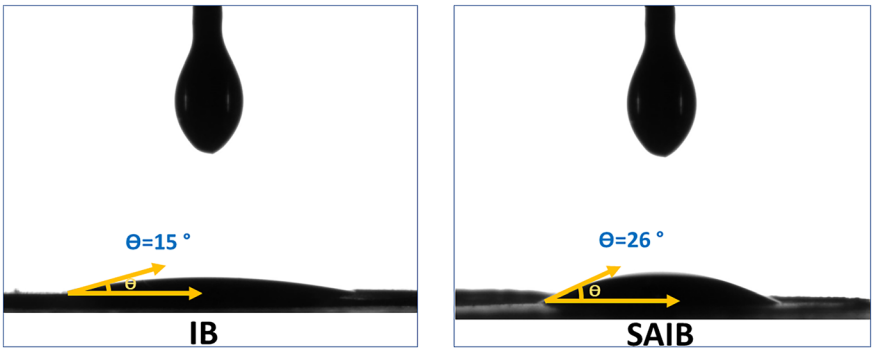

Figure 5. Contact angle images for IB and SAIB electrodes in the presence of DOLDME-LiTFSI-$LiNO_3$ electrolyte (the electrolyte is drop-casted from the top).

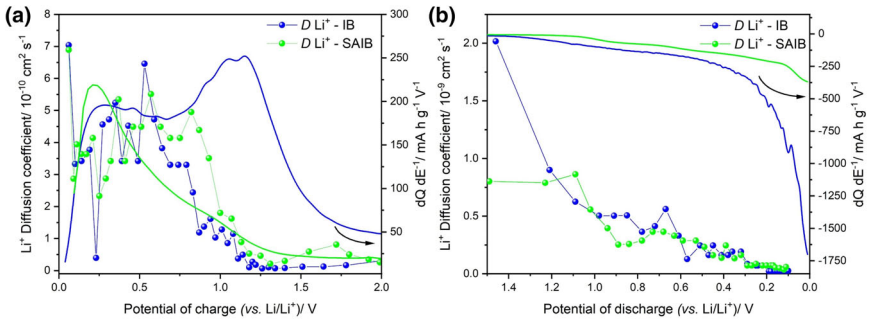

Figure 6. Apparent lithium-ion diffusion coefficients calculated from the GITT profiles during a) charge (de-lithiation) and b) discharge (lithiation) processes for IB (blue dots) and SAIB (green dots) electrodes at the 10th cycle. The right-hand side of each figure reports the values of the derivatives of the 10th discharge/charge curves for the IB and SAIB electrodes (continuous blue and green lines, respectively).

obtained a higher D_{Li+} in the case of the IB electrode at a potential of 1.5 V at the beginning of the discharge, being 2×10^{-9} $cm^2 s^{-1}$ for the IB electrode and 0.75×10^{-9} $cm^2 s^{-1}$ for the SAIB electrode. This shows that the presence of functional groups on the IB surface promotes a faster mobility for lithium ions.

The proposed mechanism for the electrochemical behavior, especially at lower current densities, of the activated and non-activated biochars in the DOLDME-LiTFSI-$LiNO_3$ electrolyte is depicted in **Scheme 1**. Since the surface of IB biochar is enriched with functional groups such as oxygen, this electrode exhibits high hydrophilicity, leading to enhanced lithium-ion mobility compared to that of SAIB. It is noteworthy that the active sites at the nanopores or edges can undergo a transformation into ether or carbonyl groups. In comparison to carbon defects, these interfacial oxygen groups exhibit lower chemical activity toward the electrolyte, preventing electrolyte decomposition during redox reactions.

The IB electrode demonstrates steady performance due to the strong interaction between the ether or carbonyl groups and the SEI layer. In contrast, the SEI film generated on the surface of SAIB may degrade during recharging because of the exfoliation of the graphite layer. Consequently, better cycling performance is expected for the IB electrode. Additionally, the oxygen groups provide more sites for lithium-ion storage, resulting in an increase in the d-spacing of graphitic layers and improving the electrode's capacity.

Furthermore, compared to materials made entirely (or mostly) of carbon, oxygen groups exhibit a stronger wetting behavior toward the ether electrolyte. This improvement enhances the lithium-ion diffusion coefficient, ensuring excellent rate performance.

2.3. LiMFS Cell Based on the IB Anode

After the electrochemical analyses of biomass-based electrodes in a half-cell configuration, IB was applied as the anode in the LiMFS cell. This cell design is particularly appealing for utilizing a low-cost, high-performance, environmentally friendly, and safe anode material as an alternative to traditional graphite and metallic lithium. Before cell assembly, the IB electrode was pre-lithiated according to the procedure discussed in Section 4. The pre-lithiation step enables the anode to function as a lithium reservoir. The voltage versus time profiles of an asymmetric lithiated IB/IB cell during a continuous galvanostatic cycle (2 h at +0.1 mA cm^{-2}, 2 h at −0.1 mA cm^{-2}) at room temperature are presented in Figure S7, Supporting Information. According to the analysis, the asymmetric cell exhibits a stable voltage over +350 h of cycling (∼±0.9 V), which suggests a reversible insertion and de-insertion of Li in the IB electrode without significant loss of lithium and resistance build-up throughout. On the other hand, adjusting the capacity ratio between the anode and cathode (i.e. cell balancing) is crucial to enhancing the performance of the LiMFS cell. Different ratios may significantly alter the cell voltage and its delivered capacity. Precise balancing is essential to avoid overcharging the battery and lithium plating at the anode, which can lead to safety issues and degrade the system's cycle life.[56] In our cell assembly, a slight excess of anode capacity (i.e., anode capacity to cathode capacity ratio is between 1.1 and 1.3, the typical ratio in LIBs, according to the stable capacity of the electrodes at low current density) has been considered. The lithiated IB/Sulfur cell was assembled in the charged state and operated upon discharge by de-intercalation of lithium ions at the IB anode and converting to lithium polysulfides at the sulfur cathode (**Figure 7**a). Thus, the LiMFS cell benefits from multiple-electron reactions, akin to lithium–sulfur batteries (Figure 7d). The IB/sulfur cell exhibits an initial discharge and charge capacity of 460 and 440 mA h g^{-1}, respectively, resulting in an ICE of 96%. The high ICE of the cell is attributed to the pre-formed SEI on the surface of the IB electrode through pre-lithiation, preventing excessive lithium consumption during this process.

The cell appears to have two inclined plateaus during discharge, occurring between 2 and 1.2 V, and one voltage plateau during charging, occurring between 1.15 and 2.2 V. The cell's average working voltage is around 1.5 V, exhibiting a stable capacity of approximately 335 mA h g^{-1} (based on sulfur active mass) with an average coulombic efficiency of 96.7% during 100 charge and discharge cycles at 0.1 C (Figure 7b). Based on the cell voltage and the delivered initial capacity, the Li_xC//Sulfur system delivers an energy density of ∼600 Wh kg^{-1} (based on sulfur mass loading). In terms of rate performance, the full

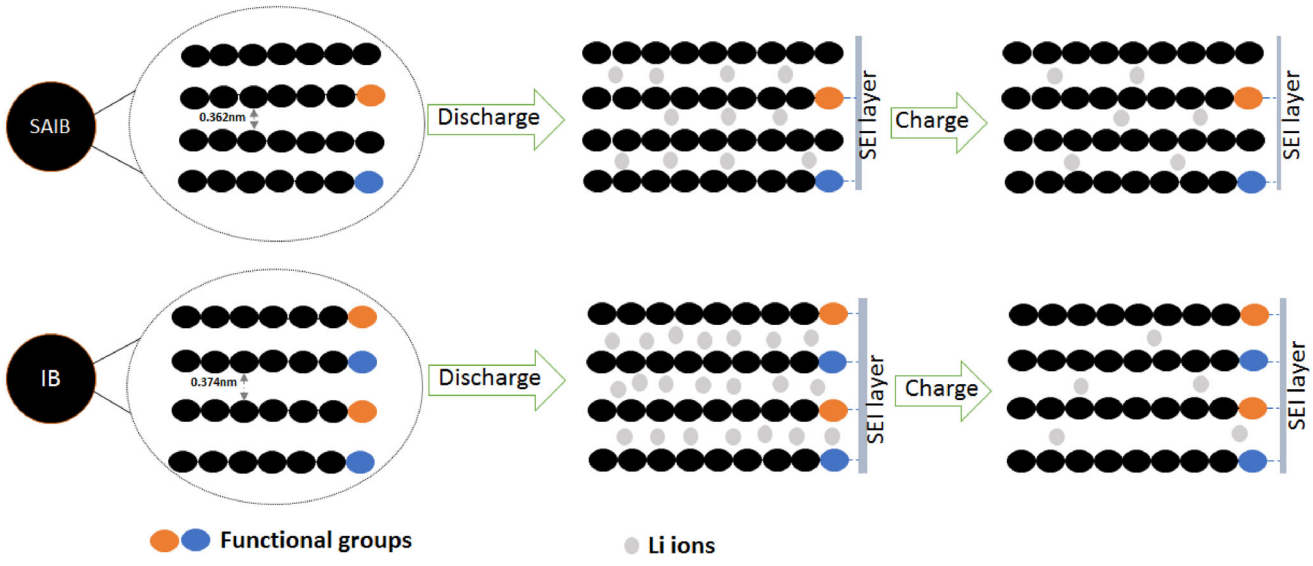

Scheme 1. The proposed mechanism for IB and SAIB electrodes in the electrolyte condition of sulfur batteries.

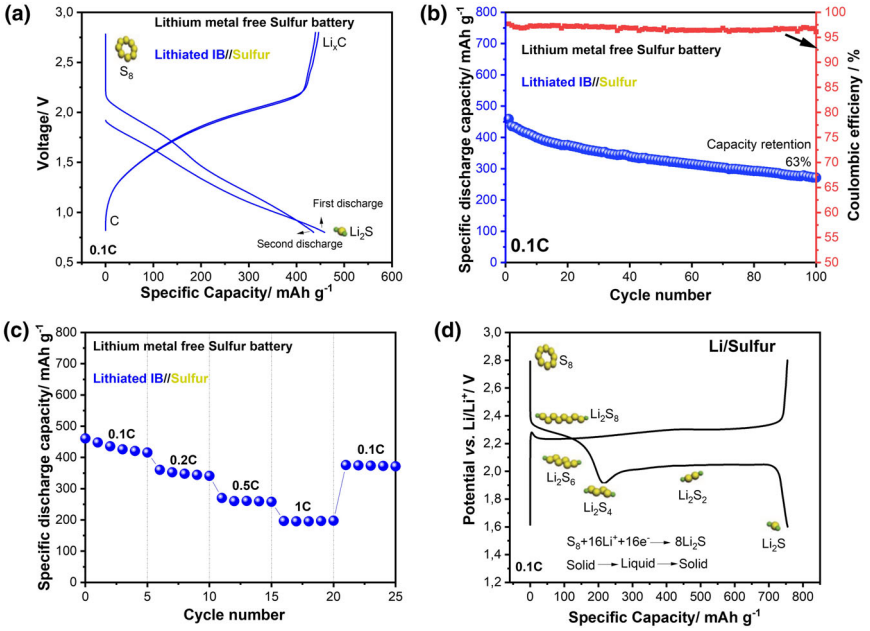

Figure 7. a) Galvanostatic charge and discharge profile, b) cycling performance, and c) rate performance of LiMFS cells based on the IB anode at 0.1, 0.2, 0.5, and 1 C (1 C = 1675 mA g^{-1}). The specific capacity of the cell is reported, considering the sulfur mass. The test is performed in the voltage range of 0.8–2.8 V at room temperature. Electrolyte: DOLDME-LiTFSI-$LiNO_3$. Anode capacity to cathode capacity ratio is ~1.3. d) Galvanostatic charge and discharge profile (50th cycle) of Li/S cell in the same electrolyte of LiMFS cell in the potential range of 1.6–2.8 V.

cell also exhibits good behavior, with specific discharge capacities of 350, 260, and 196 mA h g^{-1} at 0.2, 0.5, and 1 C, respectively (Figure 7c). This analysis reveals approximately 75% capacity retention when increasing C-rates from 0.2 to 0.5 C and from 0.5 to 1 C. Additionally, 90% of the capacity at the 5th cycle at 0.1 C is retained after 20 cycles at various C-rates, demonstrating the good reversibility of the system.

The voltage profile of the lithiated IB/Sulfur (LiMFS) cell is a superposition of the individual voltage dynamics of the lithiated IB and sulfur electrodes (against Li reference). As such, considering the non-zero average discharge voltage of the IB electrode versus Li (Figure S8a, Supporting Information), it is expected that the discharge voltage and energy of the lithiated IB/Sulfur are inferior to those of Li/S cell (Figure S8a,c, Supporting Information). This is, however, inevitable when a Li-insertion electrode is used instead of a metal electrode as the anode in a full cell. The rate-performance of the individual electrodes and that of the full cell are comparable in terms of the normalized capacity and energy versus C-rate (Figure S8b,c, Supporting Information). This observation suggests that the overall kinetic rate of lithium (de)insertion in a lithiated IB electrode is comparable to that of Li stripping/plating at the Li electrode. As such, the higher equilibrium voltage of lithium (de)insertion at the IB electrode is the main reason behind the lower discharge energy of the lithiated IB/Sulfur cell relative to the Li/S cell. Indeed, a dedicated optimization of the electrode balancing can improve the performance of the LiMFS cell, which is a topic of our future studies. For instance, side reactions in a full cell, such as SEI formation, if not controlled, will deplete the limited resource of Li in the IB electrode and shift the balancing of the cell. This needs a synergistic optimization of the initial capacity ratio of the anode and cathode and the electrolyte formulation.[57]

The EIS spectra of the LiMFS cell were measured, and the Nyquist plot is depicted in Figure S9, Supporting Information. In the fresh state, the charge transfer (R_{ct}) and SEI (R_{sei}) resistances are approximately 4 Ω and 9.8 Ω, respectively. After 25 cycles at various C-rates, R_{sei} decreases to 2.2 Ω, while R_{ct} increases to 11.9 Ω. This limited change in the cell impedance after long-term cycling highlights the robust electrochemical stability of the LiMFS system.

The cycling performance of our developed LiMFS cell, featuring an IB anode, in comparison with a Li/S cell is presented in Figure S10, Supporting Information. After 80 cycles at a rate of 0.5 C, the LiMFS cell exhibits a capacity retention of 89%, while the Li/S cell demonstrates a capacity retention of 83%. It is well known that cycling in liquid electrolytes can lead to dendrite growth on lithium-metal electrodes, potentially causing cell shorting and even fire or explosion.[58] Therefore, battery manufacturers are hesitant to use lithium metal unless the battery systems employ electrolyte media compatible with the metal. One of the primary challenges hindering the commercialization of lithium-sulfur batteries is their low cycle stability, partly attributed to the prevalent use of lithium metal as the anode.[59] Liquid electrolytes currently in use are unstable when in contact with metallic lithium, failing to form a stable SEI. Similar to lithium-oxygen cells,[60] extended cycling in Li/S batteries necessitates excessive electrolyte and lithium usage. Overall, employing a metallic lithium anode poses significant drawbacks, including dendrite formation and a low melting point, which may lead to thermal runaway and pose safety risks.

In this study, while the innovative cell utilizing a biochar anode demonstrates considerable potential as a viable energy storage system, it is essential to acknowledge the existence of technical barriers and scientific challenges that must be addressed to optimize the efficiency of the cell. One of the main challenges is related to the anode prelithiation before coupling with the sulfur cathode. Since in the LiMFS battery, the anode acts as the lithium reservoir, the complete lithiation of the anode significantly affects the overall performance of the battery. Additionally, optimizing the anode/cathode mass balancing can further improve the capacity and lifetime of the system.

Apart from these, the use of sulfur in next-generation energy storage systems still faces some critical challenges due to the inherent sluggish redox kinetics and severe polysulfide shuttle. Thus, a feasible approach should be studied and considered to guide the practical design of advanced sulfur cathodes for application in LiMFS technology.

3. Conclusion

The morphological, structural, and electrochemical characteristics of carbons derived from pyrolysis (biochar) and activation (activated biochar) processes were compared for potential applications in lithium-metal-free sulfur batteries, LiMFS. An environmentally friendly

activation method based on steam activation was employed to improve the surface area and pore size of ivy biochar (IB). In both cases, the assembled lithium half-cells demonstrated good compatibility with the state-of-the-art electrolyte of sulfur batteries, especially, the non-activated biochar cell, which provides the highest initial capacity and capacity retention over extended cycling. Differences in morphology, surface chemistry, surface area, and porosity resulted in distinct electrochemical behavior. For instance, IB with a lower specific surface area demonstrated higher initial coulombic efficiency compared to that of steam-activated ivy biochar (SAIB). Additionally, in comparison with SAIB, the IB electrode with higher quantities of oxygen-containing surface functional groups exhibited a steadier capacity due to the strong interaction between the ether or carbonyl groups and the solid electrolyte interphase (SEI) layer.

It should be pointed out that the most significant contribution to the synthesis process of IB and SAIB is the electricity and gas consumption during pyrolysis and steam activation. The synthesis of SAIB consumes additional electricity and gas, resulting in a more energy-intensive synthesis route. Therefore, from an environmental standpoint, IB with no post-treatment process has lower environmental impacts and appears to be the most promising sample for further investigation. Finally, the IB electrode was chosen for application in LiMFS cells as an innovative and green battery technology. The Li_xC//Sulfur system achieved a specific energy density of approximately 600 Wh kg^{-1} with superior cycling performance compared to the Li/S cell. Although this battery could be a very promising energy storage system, there are still some technical barriers and challenges that need to be overcome to enhance the cell performance, such as progress in the pre-lithiation strategy, very careful cell capacity balancing, and the practical design of advanced sulfur cathodes.

4. Experimental Section

Synthesis of biochar and activated biochar based on spent common ivy: Freshly harvested common ivy trimmings were dried at 105 °C and subsequently shredded in a Retsch SM100 (Retsch, Haan, Germany) cutting mill of 10 × 10 mm. Pyrolysis experiments were conducted in a modified rotary kiln reactor, type RSRC 120-1000/11 Nabertherm (Lilienthal, Germany), at 700 °C. The reactor consisted of a screw feeder (biomass input rate 350–400 g h^{-1}) that fed an indirectly heated tilted rotary kiln. The kiln rotational speed and inclination were adjusted to have a particle mean residence time of approx. 15 min.[61] Pyrolysis exhaust gases were incinerated in an afterburner.

The produced biochar was ball milled in a Retsch S1 planetary ball mill (Retsch) to increase the surface area with the obtained biochar labeled IB (i.e., Ivy Biochar). After this procedure, the biochar was placed into a home-built stainless steel (AISI 310) rotating screw reactor[62] to produce steam-activated ivy biochar, labeled SAIB. The reactor was heated up to 800 °C under a nitrogen atmosphere (70 mL min^{-1}), with a rate of 20 °C min^{-1} until reaching 700 °C when a holding time of 30 min was applied. The heating continued at 10 °C min^{-1} to minimize the temperature overshoot until the activation temperature of 800 °C was achieved. The physical activation of the biochar with steam lasted for 60 min. During this process, steam was added continuously until the steam-biochar ratio was 1:1 wt%. Afterwards, this sample was cooled under a N_2 atmosphere. Finally, both IB and SAIB powders were washed with 1 M HCl and deionized water to remove possible contaminants, with a final drying step run overnight at 110 °C.

Material characterization: CHNS elemental analysis was carried out by using a Thermo Electron Flash EA1112 elemental analyzer (ThermoFisher Scientific, Waltham, MA, USA) to quantify the contents of the main heteroatoms in the samples. The oxygen content was then calculated by removing both the ash content (from TGA analysis) and the C, H, N, and S content according to the ASTM-D2866-94 protocol.[63] The surface functionality was investigated through attenuated total reflection (ATR) (MIRacle ATR, PIKE Technologies) coupled to a Fourier transform infrared spectroscopy (FTIR) (Vertex 70v FT-IR, Bruker). An X-ray diffractometer (XRD, Malvern PANalytical Empyrean) outfitted with a 1.8 kW CuK-sealed ceramic tube and a Renishaw in-Via Micro Raman system with a 532 nm laser source were used to determine the crystallinity, mineral content, and degree of order/disorder in the non-activated and activated biochars. Their morphology was examined using a JEOL JSM-6490LA SEM Analytical (low-vacuum) scanning electron microscope (SEM) and a JEOL JEM-1400plus-120Kv Transmission Electron Microscope (TEM) equipped with Energy Dispersive X-ray spectroscopy (EDX).

The IB and SAIB surface morphologies were analyzed via N_2/CO_2 adsorption and desorption at 77 K with a Tristar II 3020 surface area analyzer (Micromeritics, Norcross, USA). Prior to the measurements, the samples were dried under nitrogen flow at 150 °C for 16 h. The specific surface area (S_{BET}) was calculated via the Brunauer–Emmett–Teller theory.

Electrode preparation, cell assembly, and electrochemical measurements: The IB and SAIB electrodes were prepared according to the protocol reported in a previous work of ours.[19] The active mass loading of the anode electrodes was in the range of 2–3 mg cm^{-2} (thickness ~50 µm). The ether-based electrolyte employed in this work, hereafter named DOLDME-LiTFSI-$LiNO_3$, was formed by 1 mol kg^{-1} of lithium bis(trifluoromethane)sulfonimide salt (LiTFSI) and 1% of lithium nitrate ($LiNO_3$) dissolved in a mixture of 1:1 w/w of 1,3-dioxolane (DOL) and 1,2-dimethoxyethane (DME). The amount of electrolyte was kept constant at ≈10 $\mu L_{electrolyte}$ $mg_{active\ material}^{-1}$ for all the fabricated cells.

For the half-cell analyses, lithium chips (15.6 mm, MTI Corporation) were used as reference and counter electrodes. The cells were assembled in an argon-filled glovebox with H_2O and O_2 levels lower than 0.1 ppm. The Li/IB and Li/SAIB half-cells were analyzed with a constant current (CC) protocol in the potential range of 0.01–3.00 V. The cyclic voltammetry (CV) measurements of IB and SAIB in the half-cell configuration were carried out at different scan rates (from 5 to 0.1 mV s^{-1}) in the potential range of 0.01–3.00 V. During the galvanostatic intermittent titration technique (GITT) analysis, the IB and SAIB-based half-cells were discharged/charged at 50 mA g^{-1} with a current pulse duration of 10 min and an interval resting time of 2 h. The electrochemical impedance spectroscopy (EIS) technique was performed at open circuit potential (OCP) for the half-cells in the frequency range from 10 kHz to 10 mHz with a 10 mV amplitude. Lithium (de) insertion with galvanostatic analysis for the IB electrode was conducted by applying a current density of 0.1 mA cm^{-2} in the asymmetrical coin cell at room temperature to assess the electrode's stability under dynamic conditions. Finally, the contact angles between the electrolyte and IB/SAIB electrodes were measured by employing an OCAH 200 contact angle goniometer.

In the full-cell (LiMFS) configuration, the sulfur electrode was coupled with the IB electrode only, as this kind of electrode had shown better performance than the SAIB electrode in the half-cell configuration. The sulfur electrode was prepared by combining 60 wt% of sulfur powder (Sigma Aldrich), 30 wt% of carbon super C65 (Imerys), and 10 wt% of binder (polyvinylidene difluoride (PVdF) from Solvay). *N*-methyl-2-pyrrolidone (NMP, Sigma Aldrich) was added as a solvent for the slurry preparation, which was then ball-milled for 15 min at the speed of 1000 rpm, casted by doctor-blade onto an aluminum foil, and dried for 12 h at 60 °C. The electrode foil was punched to form 10 mm diameter disks, resulting in an active mass loading (sulfur) of around 1–1.1.6 mg cm^{-2}. The Li/Sulfur cell was also assembled and galvanostatically charged and discharged at 0.1 and 0.5 C (1 C = 1675 mA g^{-1}) in the potential range of 1.6–2.8 V.

In LiMFS full-cell configuration, the IB electrode (d = 12.6 mm and mass ~2.5 mg) was prelithiated to provide a source of lithium for the system. The prelithiation was realized by applying a current density of 0.1 A g^{-1} (based on the IB active mass) while the anode was immersed in the aforementioned ether-based electrolyte. The detailed information on the prelithiation is reported elsewhere.[19] The IB electrode was then rinsed with DME solvent in an argon-filled glove box after half-cell disassembly and dried for 30 min. Afterward, a sulfur cathode with a mass of 1.15 and 1.6 mg cm^{-2} (d = 10 mm) was selected to be coupled with the IB anode. This choice was dictated by the requirement of maintaining a proper capacity balance between the anode and the cathode, with an anode-to-cathode capacity ratio between 1.1 and 1.3. Finally, a LiMFS cell adopting IB as an anode was electrochemically analyzed in the voltage range of 0.8–2.8 V at 0.1, 0.2, 0.5, and 1 C. All the electrochemical characterizations were done at room temperature by employing a BCS-805 multichannel battery unit by BioLogic.

Acknowledgements

The authors would like to acknowledge the technicians who performed analyses in this study: Gianfabio Mangione and Thomas Vranken for Raman Analysis, Dr. Bjorn Joos, and Martine Vanhamel for BET and FTIR analyses. We also thank Luca Leoncini for STEM-EDX measurements. This work was financially supported by the Special Research Fund (BOF23PD03; P. Salimi) and the Research Foundation Flanders (FWO SB-1S92022N; W. Vercruysse).

Conflict of Interest

The authors declare no conflict of interest.

Supporting Information

Supporting Information is available from the Wiley Online Library or from the author.

Keywords

activated biochar, biochar, electrochemical performance, functional groups, lithium-metal-free sulfur batteries

Received: November 22, 2023
Revised: February 20, 2024
Published online: March 16, 2024

[1] D. Tong, D. J. Farnham, L. Duan, Q. Zhang, N. S. Lewis, K. Caldeira, S. J. Davis, *Nat. Commun.* **2021**, DOI: 10.1038/s41467-021-26355-z.
[2] S. Javadian, P. Salimi, H. Gharibi, A. Fathollahi, E. Kowsari, J. Kakemam, *J. Iran. Chem. Soc.* **2019**, *16*, 2123.
[3] A. Masias, J. Marcicki, W. A. Paxton, *ACS Energy Lett.* **2021**, *6*, 621.
[4] S. Hamidi, K. Askari, P. Salimi, *New J. Chem.* **2023**, *47*, 12085.
[5] J. Jiang, Q. Fan, S. Chou, Z. Guo, K. Konstantinov, H. Liu, J. Wang, *Small* **2019**, *1903934*, 1.
[6] L. Zhou, D. L. Danilov, F. Qiao, J. Wang, H. Li, R. A. Eichel, P. H. L. Notten, *Adv. Energy Mater.* **2022**, DOI: 10.1002/aenm.202202094.
[7] A. Manthiram, Y. Fu, S. Chung, C. Zu, Y. Su, *Chem. Rev.* **2014**, *114*, 11751.
[8] L. Wang, Z. Schnepp, M. M. Titirici, *J. Mater. Chem. A* **2013**, *1*, 5269.
[9] J. Wang, P. Nie, B. Ding, S. Dong, X. Hao, H. Dou, X. Zhang, *J. Mater. Chem. A* **2017**, *5*, 2411.
[10] P. Salimi, S. Javadian, O. Norouzi, H. Gharibi, *Environ. Sci. Pollut. Res.* **2017**, *24*, 27974.
[11] P. Salimi, K. Askari, O. Norouzi, S. Kamali, *J. Electron. Mater.* **2019**, *48*, 951.
[12] W. Lv, F. Wen, J. Xiang, J. Zhao, L. Li, L. Wang, Z. Liu, Y. Tian, *Electrochim. Acta* **2015**, *176*, 533.
[13] I. Kovalenko, B. Zdyrko, A. Magasinski, B. Hertzberg, Z. Milicev, R. Burtovyy, I. Luzinov, G. Yushin, *Science* **2011**, *334*, 75.
[14] H. Parsimehr, A. Ehsani, S. A. Payam, *Biomass Convers. Biorefinery* **2022**, *18*, 100190.
[15] Y. Yao, F. Wu, *Nano Energy* **2015**, *17*, 91.
[16] O. Norouzi, P. Salimi, F. Di Maria, S. E. M. Pourhosseini, F. Safari, **2019**, 233.
[17] S. Marzeddu, A. Cappelli, A. Ambrosio, M. A. Décima, P. Viotti, M. R. Boni, *Land* **2021**, *10*, 1256.
[18] P. Salimi, E. Venezia, S. Taghavi, S. Tieuli, L. Carbone, M. Prato, M. Signoretto, J. Qiu, R. Proietti Zaccaria, *Energy Environ. Mater.* **2023**, DOI: 10.1002/eem2.12567.
[19] P. Salimi, S. Tieuli, S. Taghavi, E. Venezia, S. Fugattini, S. Lauciello, M. Prato, S. Marras, T. Li, M. Signoretto, P. Costamagna, R. Proietti Zaccaria, *Green Chem.* **2022**, *24*, 4119.
[20] W. Vercruysse, B. Noppen, M. Jozefczak, M. Huybrechts, E. Derveaux, B. Vandecasteele, A. Cuypers, W. Marchal, D. Vandamme, *ACS Sustain. Chem. Eng.* **2023**, *11*, 14267.
[21] E. Sierocinski, F. Holzinger, J. F. Chenot, *Eur. J. Clin. Pharmacol.* **2021**, *77*, 1113.
[22] T. Sternberg, H. Viles, A. Cathersides, M. Edwards, *Sci. Total Environ.* **2010**, *409*, 162.
[23] R. W. F. Cameron, J. Taylor, M. Emmett, *Build. Environ.* **2015**, *92*, 111.
[24] W. Vercruysse, J. Smeets, T. Haeldermans, B. Joos, A. Hardy, P. Samyn, J. Yperman, K. Vanreppelen, R. Carleer, P. Adriaensens, W. Marchal, D. Vandamme, *J. Anal. Appl. Pyrolysis* **2021**, *159*, 105294.
[25] N. L. Panwar, A. Pawar, *Biomass Convers. Biorefinery* **2020**, *12*, 925.
[26] G. Vázquez, G. Antorrena, J. Gonzalez, S. Freire, *Holzforschung* **1997**, *51*, 158.
[27] Z. Yang, H. Peng, W. Wang, T. Liu, *J. Appl. Polym. Sci.* **2010**, *116*, 2658.
[28] G. Bekiaris, G. Koutrotsios, P. A. Tarantilis, C. S. Pappas, G. I. Zervakis, *J. Mater. Cycles Waste Manag.* **2020**, *22*, 1027.
[29] G. Müller, C. Schöpper, H. Vos, A. Kharazipour, A. Polle, *Bioresources* **2009**, *4*, 49.
[30] A. M. Raspolli Galletti, A. D'Alessio, D. Licursi, C. Antonetti, G. Valentini, A. Galia, N. Nassi O Di Nasso, *J. Spectrosc.* **2015**, 719042.
[31] T. Haeldermans, J. Claesen, J. Maggen, R. Carleer, J. Yperman, P. Adriaensens, P. Samyn, D. Vandamme, A. Cuypers, K. Vanreppelen, S. Schreurs, *J. Anal. Appl. Pyrolysis* **2019**, *138*, 218.
[32] Y. Liu, Z. He, M. Uchimiya, *Mod. Appl. Sci.* **2015**, *9*, 246.
[33] P. González-García, S. Gamboa-González, I. Andrade Martínez, T. Hernández-Quiroz, *Environ. Prog. Sustain. Energy* **2020**, DOI: 10.1002/ep.13366
[34] L. Huang, Y. Sun, W. Wang, Q. Yue, T. Yang, *Chem. Eng. J.* **2011**, *171*, 1446.
[35] C. Marino, J. Cabanero, M. Povia, C. Villevieille, *J. Electrochem. Soc.* **2018**, *165*, A1400.
[36] N. Song, N. Guo, C. Ma, Y. Zhao, W. Li, B. Li, *Molecules* **2023**, *28*, 3595.
[37] P. Salimi, O. Norouzi, S. E. M. Pourhoseini, P. Bartocci, A. Tavasoli, F. Di Maria, S. M. Pirbazari, G. Bidini, F. Fantozzi, *Renew. Energy* **2019**, *140*, 704.
[38] H. Moon, A. Innocenti, H. Liu, H. Zhang, M. Weil, M. Zarrabeitia, S. Passerini, *ChemSusChem* **2022**, *16*, e202201713.
[39] C. Quan, R. Su, N. Gao, *Int. J. Energy Res.* **2020**, *44*, 4335.
[40] H. Xie, Z. Wu, Z. Wang, N. Qin, Y. Li, Y. Cao, Z. Lu, *J. Mater. Chem. A* **2020**, *8*, 3606.
[41] A. Tomczyk, Z. Sokołowska, P. Boguta, *Rev. Environ. Sci. Biotechnol.* **2020**, *19*, 191.
[42] Y. Jia, S. Shi, J. Liu, S. Su, Q. Liang, X. Zeng, T. Li, *Appl. Sci.* **2018**, *8*, 1019.
[43] K. Xu, Y. Li, J. Xiong, X. Ou, W. Su, G. Zhong, C. Yang, *Front. Chem.* **2018**, DOI: 10.3389/fchem.2018.00366.
[44] S. Guo, Y. Chen, L. Shi, Y. Dong, J. Ma, X. Chen, H. Song, *Appl. Surf. Sci.* **2018**, *437*, 136.
[45] Z. Nie, Y. Huang, B. Ma, X. Qiu, N. Zhang, X. Xie, Z. Wu, *Sci. Rep.* **2019**, *9*, 15032.
[46] L. Carbone, M. Gobet, J. Peng, M. Devany, B. Scrosati, S. Greenbaum, J. Hassoun, *J. Power Sources* **2015**, *299*, 460.
[47] N. Elgrishi, K. J. Rountree, B. D. McCarthy, E. S. Rountree, T. T. Eisenhart, J. L. Dempsey, *J. Chem. Educ.* **2018**, *95*, 197.
[48] Z. Parviz, P. Salimi, S. Javadian, H. Gharibi, A. Morsali, E. Bayat, L. Leoncino, S. Lauciello, R. P. Zaccaria, **2022**, DOI: 10.1021/acsaem.2c02821.
[49] Z. Nie, Y. Huang, B. Ma, X. Qiu, N. Zhang, X. Xie, Z. Wu, *Sci. Rep.* **2019**, *9*, 1.
[50] Y. Wan, Y. Liu, D. Chao, W. Li, D. Zhao, *Nano Mater. Sci.* **2023**, *5*, 189.
[51] X. Lin, Y. Liu, H. Tan, B. Zhang, *Carbon N. Y.* **2020**, *157*, 316.
[52] Y. Morikawa, S. Ichi Nishimura, R. Ichi Hashimoto, M. Ohnuma, A. Yamada, *Adv. Energy Mater.* **2020**, DOI: 10.1002/aenm.201903176.
[53] K. Yu, J. Li, H. Qi, C. Liang, *Diam. Relat. Mater.* **2018**, *86*, 139.
[54] W. G. Morais, M. M. Leite, R. M. Torresi, *J. Electroanal. Chem.* **2021**, *897*, 115595.
[55] S. Alvin, H. S. Cahyadi, J. Hwang, W. Chang, S. K. Kwak, J. Kim, *Adv. Energy Mater.* **2020**, *10*, 2000283.

[56] A. Benítez, D. Di Lecce, G. A. Elia, Á. Caballero, J. Morales, J. Hassoun, *ChemSusChem* **2018**, *11*, 1512.
[57] H. Hamed, B. G. Choobar, S. Hamtaei, J. D. Haen, B. Vermang, M. Safari, *J. Electrochem. Soc.* **2024**, *171*, 020510.
[58] M. Agostini, J. Hassoun, J. Liu, M. Jeong, H. Nara, T. Momma, T. Osaka, Y. K. Sun, B. Scrosati, *ACS Appl. Mater. Interfaces* **2014**, *6*, 10924.
[59] J. Brückner, S. Thieme, F. Böttger-Hiller, I. Bauer, H. T. Grossmann, P. Strubel, H. Althues, S. Spange, S. Kaskel, *Adv. Funct. Mater.* **2014**, *24*, 1284.
[60] Z. Peng, S. A. Freunberger, Y. Chen, P. G. Bruce, *Science* **2012**, *337*, 563.
[61] T. Haeldermans, M. A. Lataf, G. Vanroelen, P. Samyn, D. Vandamme, A. Cuypers, K. Vanreppelen, S. Schreurs, *Powder Technol.* **2019**, *354*, 392.
[62] K. Vanreppelen, S. Vanderheyden, T. Kuppens, S. Schreurs, J. Yperman, R. Carleer, *Waste Manag. Res.* **2014**, *32*, 634.
[63] American Standard of Testing Material, *Astm D 2866–11* **2011**, DOI: 10.1520/D2866-11